Singly-twinned growth of Si crystals upon chemical modification

Saman Moniri,[1] Xianghui Xiao,[2,*] and Ashwin J. Shahani[3,†]

[1]*Department of Chemical Engineering, University of Michigan, Ann Arbor, Michigan 48109, USA*

[2]*X-ray Science Division, Advanced Photon Source, Argonne National Laboratory, Lemont, Illinois 60439, USA*

[3]*Department of Materials Science and Engineering, University of Michigan, Ann Arbor, Michigan 48109, USA*

(Received 17 February 2020; accepted 2 June 2020; published 19 June 2020)

During crystallization a continuum of patterns could emerge due to the interplay of growth kinetics, material or solution chemistry, and crystallographic defects. The coherent twin boundary is widely known to catalyze growth in pristine crystals including polycrystalline Si. Much remains unknown about the impact of changing the chemical environment of the crystallization process through the deliberate addition of trace metallic species—termed chemical modification. Pristine Si has been reported to grow through the classical model of two parallel twin planes acting in concert to enable steady-state propagation of the solid-liquid interfaces. Here, we achieve a vision on the growth process via *in situ* synchrotron x-ray microtomography and further corroborated by *ex situ* crystallographic investigation. We find that steady-state growth is impossible in chemically modified alloys that consist of trace (0.1 wt.%) Sr. This is because the Sr modifier poisons the concave re-entrant grooves, thereby deactivating the advantage of the twin-plane re-entrant edge mechanism and leading to a singly-twinned interface. This study may serve as a proxy to chemically modified crystallization pathways of eutectic Si in Al-Si alloys and, more broadly, as a framework for the crystallization-mediated synthesis of materials.

DOI: 10.1103/PhysRevMaterials.4.063403

I. INTRODUCTION

Understanding the relationship between the distribution of chemical impurities and microstructural defects—including grain boundaries—in crystals is of paramount importance for engineering new or improved materials for a wide variety of applications, including structural [1,2], electronic [3,4], and energy [5]. An important class of grain boundaries is the twin plane along which two crystals share the same lattice sites and intergrow through certain symmetry operations, and recent works provide key insights into the twin-forming process [6] and its impact on grain growth [7]. The use of growth modifiers in natural, biological, and synthetic crystallization is a common strategy to control growth and achieve more desirable physicochemical properties [8–12]. For structural materials, such as eutectic alloys, chemical modification through the addition of trace, typically metallic elements to the feedstock alloys during crystallization often improves the mechanical properties of growing crystals from a melt, for instance ductility and strength [13–18] of cast alloys. This is due to a combination of structural refinement [13,16] as well as morphological and topological changes during solidification [12]; Ref. [19] provides a review on the microstructural effects of chemical modification. While it is known that impurities such as those deliberately added [9,10,12,14,20] through chemical modification tend to segregate to grain boundaries [1,21] with dramatic consequences for the physical behavior of the material [8,12,19], the origins behind such drastic microstructural changes upon crystallization remain elusive.

Several models have been proposed since the 1960s and onwards to explain the mechanisms behind chemically modified crystallization. These models are often in relation to the growth of eutectic Si in Al-Si alloys whose brittleness and coarse microstructure in pristine (unmodified) state is the main reason for the poor mechanical properties of the as-cast alloy, such as premature crack initiation and fracture in tension [22]. Among these proposed models are those that describe the growth of the faceted Si phase largely based on geometric considerations involving the impurity atoms. The *twin plane re-entrant edge* (TPRE) growth mechanism (*vide infra*) describes the growth of the faceted phase facilitated by {111} $\Sigma 3$ twins [23,24]. TPRE is thought to dominate for slow cooling rates in unmodified alloys. According to the *poisoning of the TPRE* mechanism, growth of the faceted phase is more isotropic due to selective adsorption of the modifier atoms or clusters at the twin-liquid interface (i.e., deactivating the advantage of the TPRE mechanism) [25]. In the *impurity-induced twinning* (IIT) mechanism, the modifier atoms adsorb instead at the {111} step surfaces of the faceted phase, and the associated change in the stacking sequence facilitates the formation of frequent twins and locally enables growth in multiple ⟨112⟩ directions [26]. That is, both IIT and the poisoning of TPRE involve adsorption of the modifier at the Si-liquid interfaces, however, the former leads to twin formation and the latter to twin suppression.

The TPRE growth model for crystallization of a twinned diamond cubic crystal was independently proposed by Wagner [23] and Hamilton and Seidensticker [24], hereafter referred to as WHS. The model is based on enhanced nucleation at the $\Sigma 3$ twin-liquid interface. According to this model,

*Present address: National Synchrotron Light Source II, Brookhaven National Laboratory, Upton, NY 11973, USA.

†Corresponding author: shahani@umich.edu

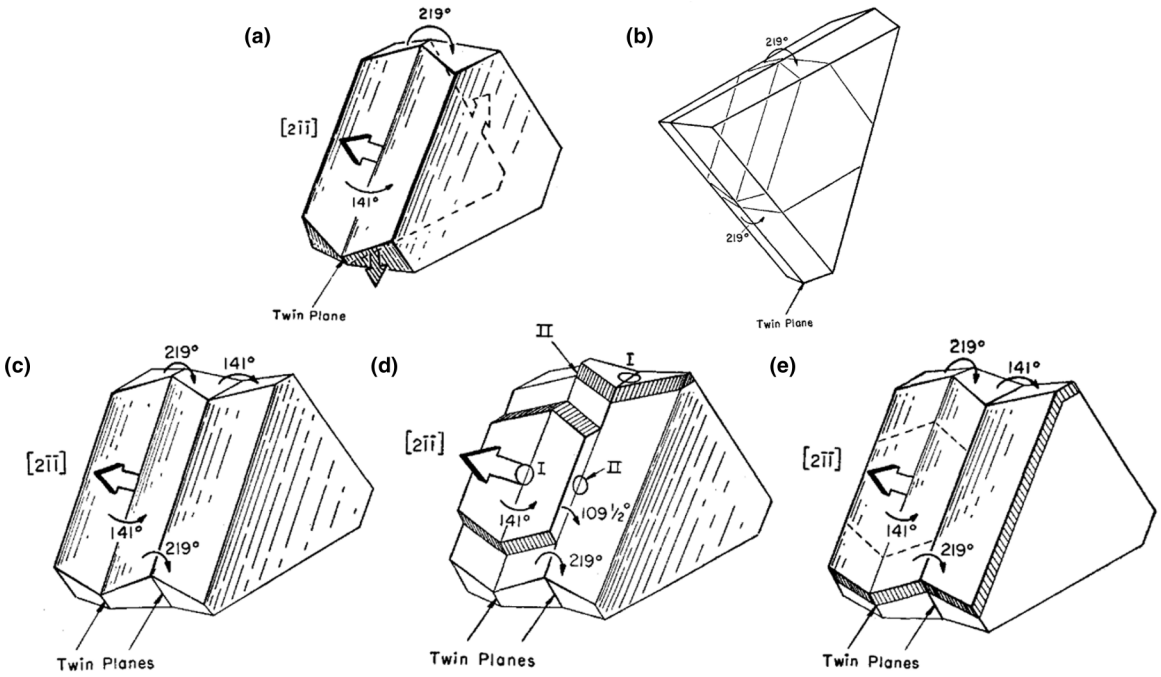

FIG. 1. Schematics of faceted crystal growth with singly- and doubly-twinned interface, according to Wagner [23] Sand Hamilton and Seidensticker [24]. (a),(b) Growth of a crystal with a single twin boundary. (a) The crystal is bounded by {111} habit planes, and a 141° re-entrant corner (type I) appears where the twin intersects the solid-liquid interface. Growth proceeds in ⟨112⟩ directions (arrows) upon nucleation at the re-entrant groove, compared to the flat {111} habit planes. (b) Growth terminates by the vanishing of the re-entrant grooves and subsequent formation of a triangular mound projecting into the melt. (c)–(e) Growth of a crystal with two parallel twin planes. (c) The doubly-twinned crystal is bounded by {111} habit planes and contains a type-I re-entrant groove. Nucleation readily occurs at the re-entrant groove as opposed to the flat {111} planes, similar to the case of singly-twinned crystal in (a). (d) At the neighboring twin the new layer creates a second re-entrant corner (type II) with an angle of 109.5°. (e) The type-II corner enables the continuous propagation of the crystal in the ⟨112⟩ direction. Unlike in the singly-twinned interface in (a), the type-I corner does not disappear during growth and no triangular mounds appear upon the termination of growth. Figure reproduced with permission from Ref. [24].

nucleation occurs at the 141° concave basin, termed type-I re-entrant groove, which is formed by the intersection of {111} interfaces on either side of the twin defect. Figure 1(a) shows the shape of a faceted crystal with a single twin plane, which contains three such re-entrants along ⟨211⟩ growth directions. Nucleation of new solid layers occurs readily at these re-entrants compared to the ⟨111⟩ flat surfaces, given that adsorption is more favorable on the groove (local coordination number of four) than on the {111} plane (coordination number 3). Therefore, growth occurs preferentially along the three re-entrant grooves and terminates upon the disappearance of the re-entrants, and the crystal attains triangular 60° corners, as shown in Fig. 1(b).

The above mechanism alludes to the requirement of a multiply twinned interface that mediates growth until, e.g., depletion of the melt. The WHS growth model of a {111}-bounded crystal with two parallel twin planes, shown schematically in Figs. 1(c)–1(e), entails rapid growth at the type-I re-entrant corner similar to the above description of a crystal with one twin. The nucleated layer propagates to the neighboring, parallel twin and subsequently forms a new re-entrant corner with an angle of 109.5° termed a type-II re-entrant. The type-II re-entrant groove alleviates the shortage of nucleation sites brought about by the formation of ridge (convex) structures during growth, thus enabling a continuous propagation of the crystal [Fig. 1(d)] until the solid attains its original shape [Fig. 1(e)]. Such concerted growth mediated by the two parallel twins proceeds in all three ⟨211⟩ directions. The key distinction between the growth of parallel-twinned and singly-twinned interfaces is that the type-II re-entrant in the former enables the cyclic, steady-state growth to proceed in the ⟨211⟩ directions with a nonvanishing type-I re-entrant.

Here, we investigate whether the formation of Si crystals in an Al-Si-Cu liquid follows the classical models mentioned above in the presence of trace modifiers. We do so by utilizing *in situ* x-ray microtomography to follow the evolution of solid-liquid interfaces as a function of time. In comparison, most previous assessments of Si modification are based on quenched specimens. Our four-dimensional (4D) (time- and 3D space-resolved) data reveal that the particles attain a more convex geometry during growth, from an initially concave-like curvature. We attribute this morphological instability to the selective poisoning of the concave re-entrant groove by the modifying agent, suggesting that the poisoning of TPRE mechanism is operative. In itself, the variable convexity of Si particles during growth provides evidence that growth does not occur under steady-state conditions. Subsequent investigations of grain-boundary characteristics and twinned interface of fully solidified Si particles in both modified and unmodified alloys show that chemical modification allows non-steady-state growth to occur with a single twin boundary at the center of the Si particle. For unmodified Si, steady-state

growth proceeds through the formation and persistence of doubly-twinned interface between the grains of Si [27]. We find that modifier clusters can readily nucleate at the re-entrant groove, owing to a nucleation barrier that is ∼50% smaller than on {111} habit planes, thereby blocking the continuous propagation of the twin boundary. Taken altogether, these insights shed light on the impact of dopants and impurities on the growth of crystals as well as their defect distributions.

II. METHODS

A. X-ray microtomography

Sample preparation. Alloy buttons of nominal composition Al–32 wt.% Si–15 wt.% Cu–0.1 wt.% Sr were cast *via* vacuum arc remelting at the Materials Preparation Center at Ames Laboratory, using 5-N purity Al, 6-N purity Si, 4-N purity Cu, and 4-N purity Sr. We note that the composition of Si (32 wt.%) in the present study is the same as that in the recent report of the unmodified alloy investigated in Ref. [27]. For the synchrotron x-ray tomography (μXRT) experiments, the as-prepared alloy buttons were cut in the shape of cylindrical rods of 1 mm diameter by 5 mm length via electrical discharge machining.

Beamline setup. The μXRT experiments were conducted at the beamline 2-BM of the Advanced Photon Source at Argonne National Laboratory (Lemont, IL, USA) and largely followed those of Ref. [12]. Typical solidification experiments began with melting the sample by heating to 935 °C and maintaining isothermally until a fully liquid sample was observed in μXRT reconstructions. The homogenized melt was then cooled at a rate of 1 °C/min, thereby solidifying the primary Si crystals (below the liquidus temperature of 910 °C). Experiments ran for over 2 h (final temperature of 808 °C). Throughout the duration of the experiments, a polychromatic "pink" x-ray beam illuminated on the samples and a 20-μm-thick LuAg:Ce scintillator converted the transmitted x rays to visible light. Images were recorded by a PCO Edge CMOS camera equipped with a 10× magnifying objective to provide isotropic pixel sizes of 0.65 mm×0.65 mm. The tomographic field of view measured 2560×600 pixels (i.e., 1664 mm×390 mm). The camera frame rate and exposure time were 50 Hz and 14 ms, respectively. Given the 1-mm diameter of each sample, the temperature distribution was assumed to be uniform within the sample. During acquisition, the sample was rotated continuously at a rate of 6° per second. For each 180° rotation of the sample, 1500 projections were collected. The large number of projections (in addition to the high exposure time of 14 ms) guaranteed high-quality images. This combination of acquisition parameters optimally allowed for a temporal discretization of 20 s between consecutive 3D reconstructions. In total more than 90 000 projections and over 60 total reconstructions were collected.

Data visualization. Reconstruction of the μXRT data was performed using TomoPy, a Python-based open source framework for the processing of tomographic data [28]. Within TomoPy, the x-ray projections were first normalized by the dark- and white-field images to account for beam instabilities. Additional correction for "ring" artefacts was made via combined wavelet-Fourier filtering [29]. Subsequently, the data were reconstructed via the direct Fourier-based Gridrec algorithm [30]. The reader is referred to Ref. [28], and references therein, for further details. In order to enhance the contrast between the solid and liquid phases, and minimize any systematic image artefacts, reconstructions of the fully liquefied sample were subtracted from all other reconstructions. A representative 2D slice of 3D reconstruction, parallel to the axis of rotation of the cylinderlike sample, is given in Fig. S1 of the Supplemental Material [37]. The strong absorption contrast between the constituents (partition coefficient of Sr $\ll 1$) allows one to easily distinguish between the two coexisting phases: primary Si crystals (dark gray) and Al liquid matrix (light gray). Subsequently, the grayscale reconstructions of this region were segmented, i.e., transformed into a computable representation of their parts (liquid + Si crystals). Our segmentation algorithm, implemented in the Image Processing Toolbox™ of MATLAB R2016a, comprised of (i) multilevel thresholding, (ii) edge-based methods for finding the boundaries of "objects" (Si and Al) within images, and (iii) morphology-based methods (e.g., dilation and erosion) in order to remove speckle noise (small objects) as well as to smooth the border of large objects [31]. Figure S1 of the Supplemental Material [37] shows the edges of the segmentation output overlaid on the original reconstruction (edges of Si are yellow, and those of Al are blue). The results indicate excellent agreement with the crystals underneath. The segmented 2D images were then stacked along the third spatial dimension to reveal the 3D microstructures.

B. Electron backscatter diffraction

Sample preparation. Fresh samples with and without a chemical modifier were prepared for electron backscatter diffraction (EBSD) experiments following the same solidification parameters as the beamline experiments described above. The solidified samples were then mechanically ground and polished, which were then polished further by Xe plasma focused ion beam using a Thermo Fisher Helios G4 PFIB UXe.

Texture analysis via EBSD. Crystallographic investigation of the fully solidified Si crystals with and without chemical modification was performed using an EBSD-equipped Tescan MIRA3 scanning electron microscope. For the EBSD experiments, the beam voltage was adjusted to 30 kV; the working distance, tilt, and step size were set to 20 mm, 70° relative to normal incidence, and 0.5–2 μm, respectively. Analysis of the texture data was performed using the MATLAB toolbox MTEX [32] in order to generate orientation maps and misorientation distributions.

III. RESULTS AND DISCUSSION

A. Growth behavior of Si particles

The dynamics of chemically modified Si crystallization was captured by *in situ* μXRT. Four representative snapshots during the growth process are shown in Figs. 2(a)–2(d), where only the Si particles are colored and the Cu-enriched liquid is rendered transparent for clarity. The particles nucleate heterogeneously on the oxide skin (translucent gray) and grow into the melt. Qualitative comparison of the solid-liquid

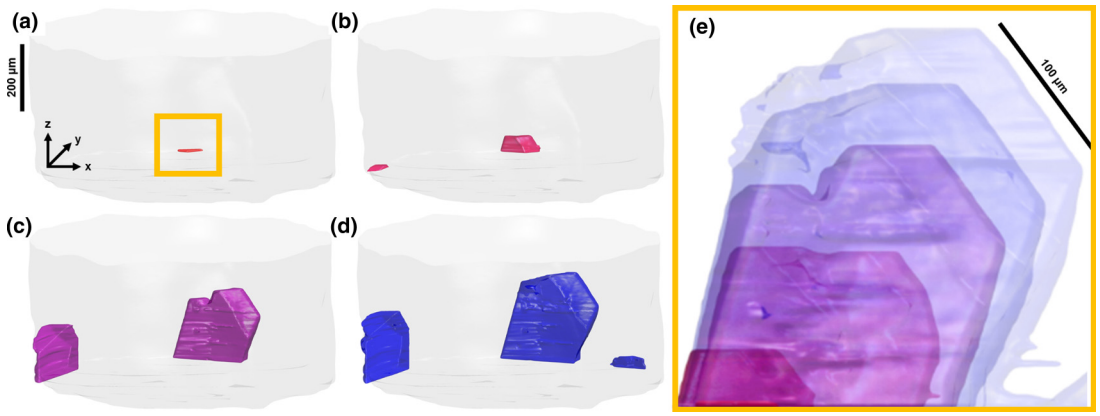

FIG. 2. 3D growth behavior of the Si particles from x-ray tomographic reconstructions. (a)–(d) The Si particles are visualized at 912, 907, 884, 879 °C (22.5, 27.5, 69, 89 min after imposing a cooling rate of 1 °C/min to the melt at 934 °C), respectively. The transparent gray wall represents the oxide skin that contained the molten specimen. The Cu-enriched liquid is rendered transparent for clarity. Si particle color reflects crystallization time, with early times in red and late times in blue. (e) A closer examination of the particle boxed in (a) suggests that Si undergoes a morphological instability during growth to attain, eventually, a convex geometry with a triangular mound projecting into the melt [cf. Fig. 1(b)]. Shown are the Si particle at six time steps: 912, 907, 890, 884, 879, 873 °C (22.5, 27.5, 44, 69, 89, and 120 min from start of cooling).

interfaces during the early [panels (a) and (b)] and late times [panels (c) and (d)] indicates a transition from a relatively flat morphology to one that features a triangular mound projecting into the melt. For subsequent analysis, we focus on the crystallization dynamics of the Si particle that forms first and which is boxed yellow in Fig. 2(a). A closer examination of the growth dynamics of this particle, shown in Fig. 2(e), indicates a continuum of polycrystalline growth forms that Si attains, undergoing a morphological instability toward an eventual convex geometry that resembles a triangular mound projecting into the melt. This morphological instability, quantified in the next section, is hypothesized (and verified below) to be the result of the disappearance of the concave re-entrant groove, and an indication of the non-steady-state growth of Si in chemically modified alloy. We note that the Si particle is not devoid of twins altogether, else its kinetic Wulff shape should resemble an octahedron bounded by {111} habit planes [33].

It is worth pointing out the difference between our 3D results and those of Ref. [27]. In the pristine (nonmodified) crystallization of Si, it was observed [27] that the type-I re-entrant (concave interface) *persists* during growth, suggesting a steady-state pathway afforded by the presence of two parallel twin planes and in which the lateral growth rate and the re-entrant nucleation rate proceed in concert. This finding illustrates that the WHS mechanism [Figs. 1(c)–1(e)] agrees with the growth of pristine Si [23,24]. The same cannot be said about the present work, cf. Fig. 2. At the macroscale, such differences in crystallization mechanisms amount to the distinction in the morphology of fully solidified Si: flat interfaces with wide terraces in the pristine crystals, and triangular corners at the growth tips in chemically modified crystals.

B. Morphology of Si particles

We quantify the observed morphological evolution of the Si crystals by computing the degree of concavity of the crystals during the late stages of growth from μXRT reconstructions. We treat *concavity* as a structural signature of the re-entrant groove, i.e., where the twin boundary intersects the solid-liquid interfaces (see Fig. 1). That is, the presence of a re-entrant groove implies that the Si crystals have a geometry that is at least partially concave. Our analysis involves generating the convex hull of the Si crystal—the intersection of all convex sets containing the crystal—and measuring the maximum normal distance from the convex hull to the crystal surface [arrow in inset (ii) of Fig. 3]. We note that, given that the crystals grow principally along their height, this choice of distance for quantifying concavity is reasonable. We limit our analysis to the same Si crystal as in Fig. 2(e). The concavity of the Si particle during growth is plotted in Fig. 3. Included in the inset are the 3D visualization of both the Si crystal (red) and the corresponding convex hull (light blue) at the three indicated time steps during growth. As the data show, the concavity initially increases and subsequently decreases as the crystal attains a more convex geometry. The initial rise in concavity distance can be explained by invoking the "growth accident" hypothesis [34], which postulates that growth twins are formed by errors in the stacking of {111} planes. Twinning, in turn, will lead to re-entrant grooves at the growth front. We postulate that the subsequent drop in concavity is due to the poisoning of the newly created re-entrant groove by the impurity Sr atoms or clusters. Upon termination of the growth process, the Si crystal is fully convex, as indicated by the "filling" of the convex hull (concavity distance of zero). The nonconstant concavity distance indicates that the Si geometry is not self-similar during growth, and that growth proceeds in a non-steady-state manner.

C. Twinning profile of fully solidified Si particles

To confirm the grain-boundary characteristics and twinned interface of the fully solidified Si particles, we conducted electron backscatter diffraction (EBSD) on both the

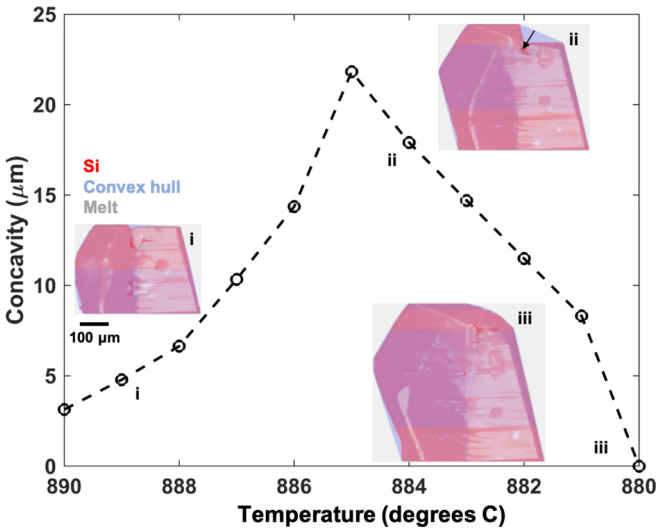

FIG. 3. Evolution of Si morphology during growth. Concavity was calculated from the μXRT results as the length of the normal vector projected from the convex hull to the crystal surface [see arrow in inset (ii)]. The analysis is limited to the single Si particle shown in Fig. 2(e), and the early times in growth are omitted due to the small size of particle at time step labeled *i*). The concavity initially increases and subsequently decreases as the crystal attains a more convex geometry. The latter suggests a disappearance of the concave re-entrant groove. Inset: Si particle (red) and its corresponding convex hull (light blue) at the three indicated time-steps (denoted *i*, *ii*, and *iii*) during growth showing that the crystal is fully convex as growth terminates, thus "filling" its convex hull.

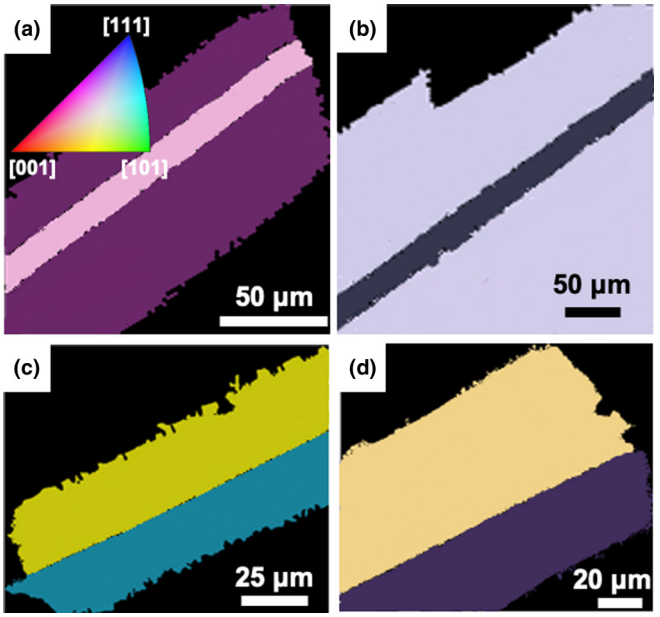

FIG. 4. The impact of chemical modification on the twinning behavior of fully solidified, primary Si particles. (a), (b) EBSD orientation maps of two representative unmodified Si particles show the existence of two parallel twin planes running across the length of the Si particles and intersecting the solid-liquid interface at the edges of the particles. (c), (d) Orientation maps of two representative chemically modified Si particles display singly-twinned interface. Similar to the unmodified case, the twin plane intersects the solid-liquid interface at the edge of the particle. In all maps, the mean crystallographic orientation of each grain of Si is colored according to the standard stereographic triangle on top-left of (a); the surrounding eutectic matrix is depicted black.

unmodified and modified Si crystals for comparison. Representative orientation maps of the two alloys are shown in Fig. 4. The mean crystallographic orientation of each grain of Si is colored according to the standard stereographic triangle on the top left of Fig. 4(a) while nonindexed regions, belonging to the Al phase and the surrounding eutectic matrix, are depicted as black. While the orientation maps provide only a qualitative intuition about the degree of crystallographic twinning as well as interlamellar spacing, they point a key striking difference in the twinning profile of the two systems: In the absence of chemical modification [Figs. 4(a) and 4(b)], the Si crystals consist of two parallel twin planes that run along the long axes of the crystals and intersect the solid-liquid interface at the crystal edges. In the chemically modified crystal [Figs. 4(c) and 4(d)], only a single twin boundary runs along the crystal that then intersects the solid-liquid interface at the crystal edges. The major distinction in the multiplicity of the twinned interface—doubly in unmodified Si, singly in modified Si—further supports the idea that the growth of modified Si crystals involves the selective poisoning of the re-entrant grooves that are formed by the intersection of the {111} Σ3 twin planes with the surface.

Quantitative analysis of the grain-boundary character involves the computation of the uncorrelated misorientation distribution function (MODF) using the discretized EBSD data taken from the interior region of a representative Si crystal (see Fig. S2 of the Supplemental Material [37]). In this analysis, only individual crystals were considered to avoid the potential ambiguity that would otherwise result if considering the entire collection of Si crystals in the fully solidified microstructure which might not have an orientation relationship. The MODF for both unmodified and modified Si is represented in Fig. S2 [37] as the distribution of both angle and axis of misorientation. In both the unmodified and modified Si, we observe only a single misorientation angle at 60° corresponding to the ⟨111⟩ misorientation axis [cf. misorientation angle plot and axis (insets) in Fig. S2 [37]]. This combination of 60°/⟨111⟩ represents the Σ3 {111} coherent twin boundary, demonstrating the high incidence of coherent twins in polycrystalline Si particles independent of chemical modification [35]. Thus, chemical modification influences not the *character* of the twin boundaries but rather their *multiplicity*.

D. Nucleation of impurity clusters on the Si crystal surfaces

The morphological instability of Si crystals during growth (Figs. 2 and 3) as observed through *in situ* μXRT experiments together with the absence of parallel twins in chemically modified Si crystals as confirmed by EBSD texture analysis (Fig. 4) point to the poisoning of the re-entrant groove in Si upon chemical modification. To verify this hypothesis, we calculate the nucleation barrier of an arbitrary impurity cluster

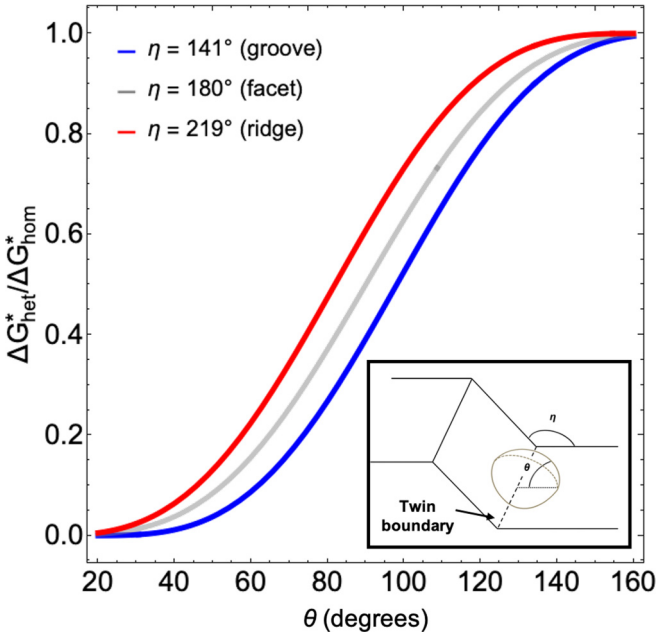

FIG. 5. Nucleation potency of impurity clusters on the Si crystal surfaces. Ratio of heterogeneous to homogeneous nucleation barriers as a function of wetting strength (contact angle θ) is plotted for a re-entrant groove, flat facet, and ridge (crystal step of angle η), computed via CNT [36]. For all contact angles, nucleation along the concave re-entrant groove is found to be more favorable than on the flat facet plane or along the convex ridge. Inset: Spherical droplet (light brown) nucleating with contact angle θ relative to the twin plane (dashed line) and step angle η.

as a function of wetting strength for a re-entrant groove, a ridge, and a flat surface [cf. Fig. 1(c)], according to classical nucleation theory (CNT) [36]; a brief sketch is provided in the Supplemental Material [37] following the derivation in Refs. [36,38]. The results, plotted in Fig. 5, indicate that impurity nucleation is more favorable at the re-entrant groove for all contact angles θ relative to the twin plane. A schematic of the nucleus and nucleant geometry is provided as an inset in Fig. 5. We point out that the spherical impurity cluster effectively "caps" the twin boundary, thereby blocking its continued propagation. This geometry is different from that of [39], which assumes that the nucleus itself is twinned. We note also that the concavity distance, as defined above, scales with the cosine of the half-angle $\eta/2$ of the crystal step angle η. Thus, for a flat facet ($\eta = 180^\circ$) concavity is identically zero; grooves and ridges ($\eta = 141^\circ$ and 219°, respectively) have equal concavity (in magnitude). Despite the latter observation, the unfavorable nucleation of impurity cluster on a ridge compared to a groove (Fig. 5) explains why one twin survives and the other is poisoned, respectively. Poisoning occurs on the re-entrant groove, which explains why the high concavity seen in Fig. 3 is short lived. Ultimately, the Si particle geometry determines the potency of impurity nucleation.

An interesting question is how exactly the Si crystal grows *around* the impurity clusters once the latter have nucleated on the re-entrant groove. The termination of a twin boundary is expected to produce dislocations [40,41] ahead of the impurity cluster in order to accommodate for the internal strain field. This question can be readily addressed through simulation, e.g., phase field crystal, which describes atomic-scale dynamics (such as dislocation creation and annihilation) on diffusive time scales [42]. We leave this open question for further research.

E. Outlook

For *in situ* monitoring of solidification processes, and particularly for metals and alloys, x-ray imaging has proven to be the method of choice. Coupling x-ray imaging with controlled solidification enables exploration of how processing conditions and alloy chemistry influence microstructural development. The distinguishing feature of this work compared to other recent studies (including *in situ* approaches) is that the latter have shed light into the late-stage growth dynamics of metallic eutectics in both the absence and presence of chemical modifiers, in an effort to corroborate models that have been proposed since the 1960s and onwards to explain the mechanisms leading to refinement and morphological evolution. Most results from these studies suggest the existence of some level of *synergism* between the chemical modifier and the twinning behavior of growing crystals. On the other hand, the present paper sheds light on a rather *antagonistic* behavior of the chemical modifier on a growing crystal (here Si), in that the modifier poisons the otherwise favorable nucleation site for the growing crystal, causing it to grow in a non-steady-state fashion. Our experimental finding is well explained on the basis of thermodynamic calculations. The non-steady-state growth proceeds via a singly-twinned interface, unlike the doubly-twinned interface of steady state growth in which the two twins act in concert to replenish the nucleation sites. This result has dramatic implications on the resultant twin densities, grain sizes, and mechanical properties of the solidified material.

At a broader level, these insights and experimental techniques could be extended to other materials classes, beyond Al-Si, that involve the interaction of "spectator" species such as modifiers, dopants, and impurities, during crystallization. As an example, the newly investigated Al-Ce alloys [43] demonstrate castability, structure, and mechanical strength similar to the near-eutectic Al-Si alloys modified by Sr; as a result, the Al-Ce alloys have been rated positively for laser additive manufacturing (no cracking or porosity). In another recent report [44], it was demonstrated that chemical modification of the feedstock alloy with grain-refining modifiers for additive manufacturing can achieve previously incompatible high-strength aluminum alloys that are crack free, equiaxed, and fine grained.

IV. CONCLUSIONS

We demonstrated the interplay of chemical modification, growth kinetics, and crystallographic defects that perturb the faceted solid-liquid interfaces upon crystallization. By combining *in situ* and *ex situ* experiments with thermodynamic calculations, we showed that chemical modification deactivates the advantage of the twin-plane re-entrant edge mechanism wherein two parallel twins enable a continuous, steady-state propagation of crystals from the melt. The chemically

modified crystallization proceeds according to the poisoning of the twin plane re-entrant groove. Consequently, the singly-twinned particles cannot grow in a steady-state fashion. These results provide insights into the relationship between the distribution of crystal defects and spectator species such as dopants or impurities, with implications to a broad range of applications including metallurgy, semiconductor processing, and additive manufacturing.

All processed data needed to evaluate the conclusions in the paper are present in the paper and/or the Supplemental Material [37]. The raw XRT projection data are publicly available in the University of Michigan Deep Blue Data repository [45].

ACKNOWLEDGMENTS

We gratefully acknowledge financial support from the NSF CAREER program under Award No. 1847855. We thank C. Reese and M. Rahman for assisting in the synchrotron experiments. We also acknowledge the University of Michigan College of Engineering for financial support and the Michigan Center for Materials Characterization for use of the instruments and staff assistance, in particular Dr. R. Kerns and Dr. N. Senabulya Muyanja for aid in EBSD experiments. This research used resources of the Advanced Photon Source, a U.S. Department of Energy (DOE) Office of Science User Facility operated for the DOE Office of Science by Argonne National Laboratory under Contract No. DE-AC02-06CH11357.

[1] I. V. Markov, *Crystal Growth for Beginners: Fundamentals of Nucleation, Crystal Growth, and Epitaxy*, 3rd ed. (World Scientific, Singapore, 2017).
[2] J. P. Buban, K. Matsunaga, J. Chen, N. Shibata, W. Y. Ching, T. Yamamoto, and Y. Ikuhara, Science **311**, 212 (2006).
[3] K. Thompson, J. H. Booske, D. J. Larson, and T. F. Kelly, Appl. Phys. Lett. **87**, 052108 (2005).
[4] J. E. Allen, E. R. Hemesath, D. E. Perea, J. L. Lensch-Falk, Z. Y. Li, F. Yin, M. H. Gass, P. Wang, A. L. Bleloch, R. E. Palmer, and L. J. Lauhon, Nat. Nanotechnol. **3**, 168 (2008).
[5] T. Buonassisi, A. A. Istratov, M. A. Marcus, B. Lai, Z. Cai, S. M. Heald, and E. R. Weber, Nat. Mater. **4**, 676 (2005).
[6] M. Song, G. Zhou, N. Lu, J. Lee, E. Nakouzi, H. Wang, and D. Li, Science **367**, 40 (2020).
[7] K. Shiga, K. Maeda, H. Morito, and K. Fujiwara, Acta Mater. **185**, 453 (2020).
[8] K. N. Olafson, R. Li, B. G. Alamani, and J. D. Rimer, Chem. Mater. **28**, 8453 (2016).
[9] S. Elhadj, J. J. De Yoreo, J. R. Hoyer, and P. M. Dove, Proc. Natl. Acad. Sci. USA **103**, 19237 (2006).
[10] J. J. De Yoreo, in *Selected Topics on Crystal Growth: 14th International Summer School on Crystal Growth*, edited by W. Wang, K. Tsukamoto, and Di Wu, AIP Conf. Proc. 1270 (AIP, Melville, NY, 2010), pp. 45–59.
[11] M. Timpel, N. Wanderka, G. S. Vinod Kumar, and J. Banhart, Ultramicroscopy **111**, 695 (2011).
[12] S. Moniri, X. Xiao, and A. J. Shahani, Sci. Rep. **9**, 3381 (2019).
[13] A. K. Dahle, K. Nogita, S. D. McDonald, C. Dinnis, and L. Lu, Mater. Sci. Eng. A **413–414**, 243 (2005).
[14] M. Timpel, N. Wanderka, R. Schlesiger, T. Yamamoto, N. Lazarev, D. Isheim, G. Schmitz, S. Matsumura, and J. Banhart, Acta Mater. **60**, 3920 (2012).
[15] P. Srirangam, S. Chattopadhyay, A. Bhattacharya, S. Nag, J. Kaduk, S. Shankar, R. Banerjee, and T. Shibata, Acta Mater. **65**, 185 (2014).
[16] J. H. Li, M. Albu, F. Hofer, and P. Schumacher, Acta Mater. **83**, 187 (2015).
[17] J. H. Li, S. Suetsugu, Y. Tsunekawa, and P. Schumacher, Metall. Mater. Trans. A **44**, 669 (2013).
[18] M. Albu, A. Pal, C. Gspan, R. C. Picu, F. Hofer, and G. Kothleitner, Sci. Rep. **6**, 31635 (2016).
[19] S. Moniri and A. J. Shahani, J. Mater. Res. **34**, 20 (2018).
[20] W. Ma, J. F. Lutsko, J. D. Rimer, and P. G. Vekilov, Nature (London) **577**, 497 (2020).
[21] B. Cai, A. Kao, P. D. Lee, E. Boller, H. Basevi, A. B. Phillion, A. Leonardis, and K. Pericieous, Scr. Mater. **165**, 29 (2019).
[22] J. E. Gruzleski, in *Production and Electrolysis of Light Metals*, edited by B. Closset (Elsevier, New York, 1989), pp. 131–141.
[23] R. S. Wagner, Acta Metall. **8**, 57 (1960).
[24] D. R. Hamilton and R. G. Seidensticker, J. Appl. Phys. **31**, 1165 (1960).
[25] M. G. Day and A. Hellawell, Proc. R. Soc. London, Ser. A **305**, 473 (1968).
[26] S. Z. Lu and A. Hellawell, Metall. Trans. A **18**, 1721 (1987).
[27] A. J. Shahani, E. Begum Gulsoy, S. O. Poulsen, X. Xiao, and P. W. Voorhees, Sci. Rep. **6**, 28651 (2016).
[28] D. Gürsoy, F. De Carlo, X. Xiao, and C. Jacobsen, J. Synchrotron Radiat. **21**, 1188 (2014).
[29] B. Münch, P. Trtik, F. Marone, and M. Stampanoni, Opt. Express **17**, 8567 (2009).
[30] B. A. Dowd, G. H. Campbell, R. B. Marr, V. V. Nagarkar, S. V. Tipnis, L. Axe, D. P. Siddons, and U. Bonse, in *Developments in X-ray Tomography II*, edited by U. Bonse (SPIE, Bellingham, WA, 1999), Vol. 3772, pp. 224–236.
[31] J. C. Russ and F. B. Neal, *The Image Processing Handbook*, 7th ed. (CRC Press Taylor & Francis, Boca Raton, 2016).
[32] F. Bachmann, R. Hielscher, and H. Schaeben, Solid State Phenom. **160**, 63 (2010).
[33] X. Yang, K. Fujiwara, K. Maeda, J. Nozawa, H. Koizumi, and S. Uda, Prog. Photovolt. Res. Appl. **22**, 574 (2014).
[34] H. Gleiter, in *Physical Metallurgy* (Elsevier, New York, 1996), pp. 843–942.
[35] S. Ratanaphan, Y. Yoon, and G. S. Rohrer, J. Mater. Sci. **49**, 4938 (2014).
[36] C. A. Sholl and N. H. Fletcher, Acta Metall. **18**, 1083 (1970).
[37] See Supplemental Material at http://link.aps.org/supplemental/10.1103/PhysRevMaterials.4.063403 for a sketch of the thermodynamic calculations.

[38] N. Senabulya and A. J. Shahani, Phys. Rev. Mater. **3**, 93403 (2019).
[39] A. D. Gamalski, P. W. Voorhees, C. Ducati, R. Sharma, and S. Hofmann, Nano Lett. **14**, 1288 (2014).
[40] J. G. Zheng, X. Pan, M. Schweizer, F. Zhou, U. Weimar, W. Göpel, and M. Rühle, J. Appl. Phys. **79**, 7688 (1996).
[41] S. Xue, Z. Fan, Y. Chen, J. Li, H. Wang, and X. Zhang, Acta Mater. **101**, 62 (2015).
[42] N. Pisutha-Arnond, V. W. L. Chan, K. R. Elder, and K. Thornton, Phys. Rev. B **87**, 014103 (2013).
[43] A. Plotkowski, O. Rios, N. Sridharan, Z. Sims, K. Unocic, R. T. Ott, R. R. Dehoff, and S. S. Babu, Acta Mater. **126**, 507 (2017).
[44] J. H. Martin, B. D. Yahata, J. M. Hundley, J. A. Mayer, T. A. Schaedler, and T. M. Pollock, Nature (London) **549**, 365 (2017).
[45] https://doi.org/10.7302/812m-d307.